SUPPLEMENTARY INFORMATION

Directed crystalline symmetry transformation of blue-phase liquid crystals by reverse electrostriction

T.-H. Lin, D.-Y. Guo, C.-W. Chen, T.-M. Feng, W.-X. Zeng, P.-C. Chen, L.-Y. Wu, W.-M. Guo, L.-M. Chang, H.-C. Jau, C.-T. Wang, T. J. Bunning, I. C. Khoo

Abstract. Note 1 discusses the roles of surface treatment and temperature in reverse-electrostriction-directed assembly (REDA) for maximizing the size of monocrystalline blue-phase liquid crystal (BPLC). **Note 2** details the numerical approach for simulating Kossel diagrams of the BPLC photonic crystals studied in this work, along with the fitting procedure to retrieve the lattice parameters a, b, c and skew angle β from a measured Kossel diagram.

Note 1: Effects of surface alignment and temperature on REDA

Figure S1 shows optical micrographs of a BPLC sandwiched between indium-tin-oxide glass windows with a patterned alignment layer. The alignment layer is a thin film of photoalignment agent brilliant yellow (from Sigma-Aldrich). A linearly polarized, continuous-wave, 457-nm laser illuminates the film within the white dashed circle. This laser, with an intensity of 110 mW/cm², aligns the brilliant-yellow molecules, establishing an in-plane easy axis for liquid crystal alignment near the interface. In **Fig. S1a**, the sample is maintained in the BPI at ~0.1°C below the BPI–BPII phase transition temperature. After applying a millisecond pulse of 1-kHz AC electric field, the initial polycrystal in the photo-aligned region transitions to a single crystal through REDA, whereas the untreated area retains a polycrystalline texture but with larger grain sizes relative to the initial state. This observation suggests that surface alignment offers a uniform direction to guide the in-plane orientation of crystal grains during REDA, thereby facilitating grain merging throughout the bulk. Next, we reset the sample through a thermal cycle (i.e., heating the BPLC to the isotropic phase, and cooling it to BPI) and bring it to a lower temperature, ~1°C below the transition temperature. **Figure S1b** shows that, the BPLC within and outside of the photo-aligned region remains polycrystalline after REDA but comprising much finer grains. This highlights the crucial role of working temperature in promoting grain merging and the formation of a large monocrystalline texture.

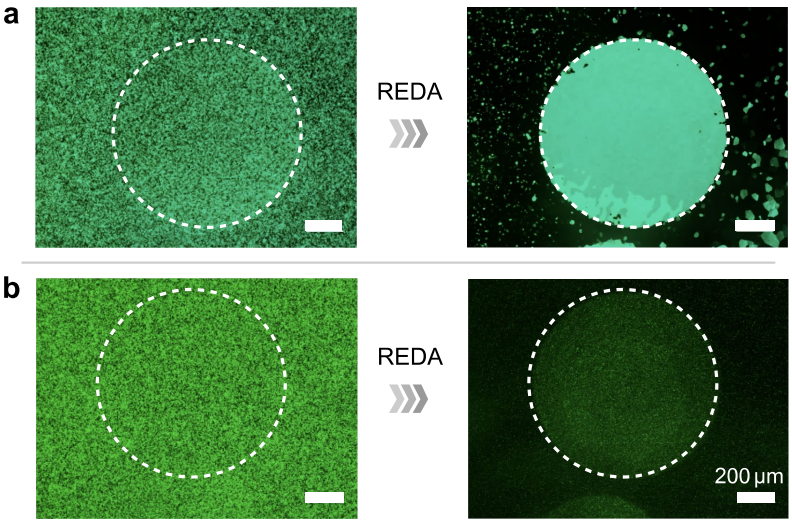

Fig. S1. Effects of surface alignment and temperature on REDA. Optical micrographs of a patterned BPLC before and after REDA, operating at **a** 0.1°C and **b** 1.0°C below the BPI–BPII phase transition temperature (32.0°C). Surface alignment is applied only within the circled area. **a** The surface alignment provides an in-plane easy axis (from left to right) for orienting the crystal grains nucleated after applying a pulsed electric field, thus facilitating their subsequent merging into a single crystal. **b** REDA becomes less effective in producing single crystals when operating away from the phase transition point.

Note 2: Extracting lattice information from reflection spectrum & Kossel diagram

The lattice structures studied in this work can be described using a set of basis vectors $\boldsymbol{a}$, $\boldsymbol{b}$, and $\boldsymbol{c}$, and the corresponding lattice parameters are the magnitudes of these vectors: $a = |\boldsymbol{a}|$, $b = |\boldsymbol{b}|$, and $c = |\boldsymbol{c}|$. $\boldsymbol{c}$ is typically aligned with the applied-field axis, cell normal, and the optical axis of the imaging system [**Fig. S2a**]. Through careful analysis, four crystal symmetries are observed: cubic, orthorhombic, tetragonal, and monoclinic. Cubic, orthorhombic, and tetragonal structures possess orthogonal basis vectors, and monoclinic structures have non-orthogonal $\boldsymbol{a}$ and $\boldsymbol{b}$ vectors. To account for this, we introduce a skew angle β, which represents the deviation from 90° of the angle formed between $\boldsymbol{a}$ and $\boldsymbol{b}$. Here we describe our methodology for extracting a, b, c and β of a BPLC sample from its reflection spectrum and Kossel diagram.

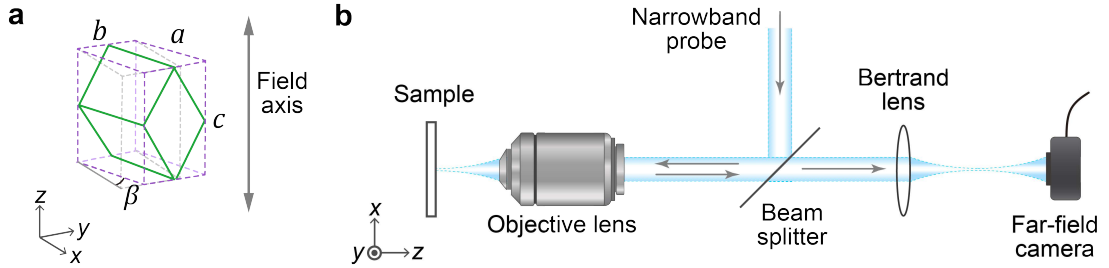

Fig. S2. Experimental setup for measuring the Kossel diagram of a BPLC sample. a Definition of lattice parameters a, b, and c, and skew angle β. **b** Experimental setup. A narrowband probe is reflected by a beam splitter and focused onto the sample by an objective lens. The reflected light from the sample is coupled back into the objective lens, passes through the beam splitter and a Bertrand lens, and arrives at a camera imaging the far field of the sample.

Figure S2b displays the schematic of the experimental setup. The sample is placed under a reflective polarizing optical microscope (Eclipse LV100 POL, Nikon), comprising a light source, a 100× objective lens, a Bertrand lens, and either a spectrometer (USB4000, Ocean Optics) or a camera (DS-Fi1, Nikon). The choice of the light source depends on the specific measurements, which will be detailed later. The sample is located at the front focal plane of a 100× objective lens. The Bertrand lens and tube lens together form a 4f imaging system. The system projects the far-field diffraction pattern of the BPLC at the back focal plane of the objective onto an image plane, where the spectrometer or the camera is positioned.

We first measure the reflection spectrum along the $\boldsymbol{c}$ axis of the BPLC (parallel to the cell normal). This is accomplished using a halogen lamp (64610 HLX, Osram) as a white-light source and an optical fiber positioned at the center of the image plane, which guides the light to the spectrometer, which has a resolution of ~0.3 nm. Lattice parameter c can be directly retrieved from the measured reflection spectrum: $c = \lambda_B / n_{avg}(\lambda_B)$, where λ_B is the center wavelength of the Bragg reflection band (or, the photonic band gap), and n_{avg} is the average refractive index at λ_B. n_{avg} of our BPLC mixture is measured using an Abbe refractometer at three different wavelengths λ [nm] in the visible and fitted with Cauchy's equation: $n_{avg} = 1.5179 + 10740/\lambda^2$ [**Fig. S3a**].

Next, we send a narrowband probe with a 5-nm bandwidth through the BPLC to generate a Kossel diffraction pattern [**Fig. S3b**]. This can be achieved by either adding a bandpass filter to the halogen lamp's output or replacing the lamp with a monochromator. We select the probe wavelength of $\lambda_S \approx 405$ nm to enable the observation of several diffraction arcs in the image plane. These arcs are commonly referred to as Kossel rings, even though parts of them are outside the field of view. The Kossel diagram captured by the camera is an orthogonal projection of the far-field diffraction on the image plane.[1] To determine the spatial frequency for each camera pixel, we calibrate our imaging system using a reflective amplitude grating

with a binary reflectivity distribution of period $d = 1.66$ μm and a monochromater that allows us to adjust the probe wavelength between 420 and 660 nm. The camera generally captures a few orders of grating diffraction. With a known probe wavelength λ_S, the diffraction angle θ is related to diffraction order m as $m\lambda_S = 2d \sin\theta$. Larger angles correspond to higher spatial frequencies. By varying the grating orientation and the probe wavelength, we establish a direct mapping between camera pixel positions and spatial frequencies.

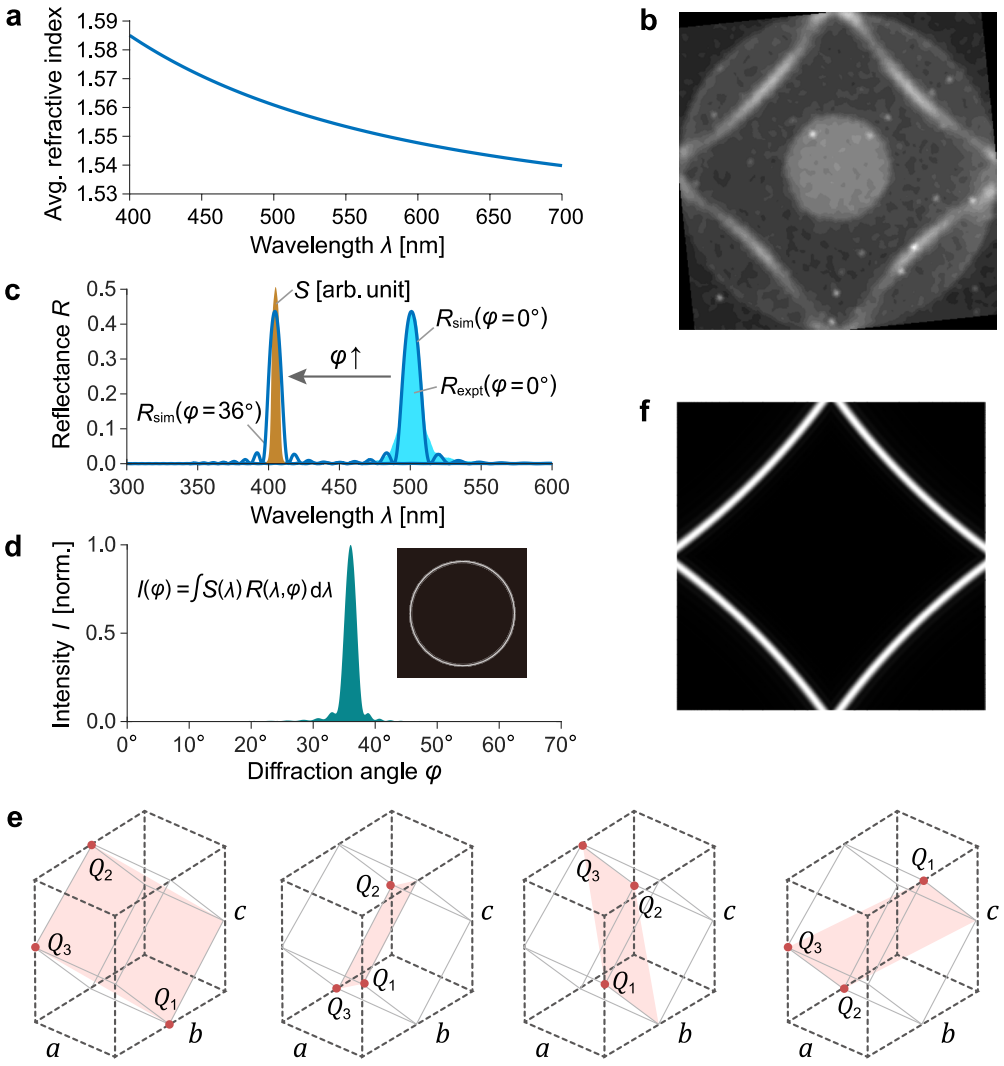

Fig. S3. Numerical reconstruction of a Kossel diagram. a Material dispersion: average (avg.) refractive index of the BPLC as a function of wavelength λ. **b** Experimentally measured Kossel diagram of a BPLC. **c** Spectra of Bragg reflection $R(\varphi, \lambda)$ (blue) and narrowband probe $S(\lambda)$ (yellow). φ is the angle to the normal of the lattice plane that reflects (or, diffracts) the narrowband probe. R_{expt}: measured reflection spectrum (light blue), R_{sim}: simulated reflection spectrum (dark blue). Reflection spectrum blue-shifts with increasing angle φ. **d** Angle-dependent intensity $I(\varphi)$ showing that strong diffraction occurs at the angle φ (36° in this example) where the Bragg reflection band significantly overlaps with the spectrum of narrowband probe. Inset: the intensity profile is a ring pattern in the Cartesian coordinates. **e** Schematic of the four lattice planes contributing to the diffraction pattern in panel **b**. Red dots: three points (Q_1, Q_2, and Q_3) on the lattice plane used to calculate the plane normal. **f** Simulated diffraction pattern matching the measured Kossel diagram in panel **b**.

The information about a, b, and β lies in the size and position of the rings in a Kossel diagram. To obtain their values, we have developed a code to numerically construct Kossel diagrams with a, b, and β as free parameters, and optimize their combination so that the generated diagram closely resembles the experimentally measured counterpart. In the measured

Kossel diagrams of our BPLC samples, there are four bright rings (or eight in the case of the monoclinic polycrystals) within the field of view. If examining a body-centered cubic (BCC) crystal with its $\boldsymbol{c}$ axis being the $[110]_{\mathrm{BCC}}$ axis, the four rings correspond to four lattice planes (101), $(10\bar{1})$, (011), and $(01\bar{1})$. Each ring corresponds to a far-field diffraction of the narrowband probe from a specific lattice plane of the examined crystal, with its normal vector denoted as $\boldsymbol{N}$. This ring pattern can be simulated using the spectrum of the narrowband light source $S(\lambda)$ and the Bragg spectrum $R(\lambda, \varphi)$ of the photonic crystal across a range of reflection angles φ with respect to $\boldsymbol{N}$ [**Fig. S3c**]. $S(\lambda)$ is measured with a resolution of 0.3 nm across a wavelength range of 300 nm to 600 nm. $R(\lambda, \varphi)$ is discretized with respect to both wavelength (λ) and reflection angle (φ), and the discretization for λ matches the resolution of $S(\lambda)$ (0.3 nm). While S is measured directly, R is computed as follows [**Fig. S3c**]. By drawing the analogy between BPLC and its 1D counterpart, cholesteric (or chiral nematic), the Bragg spectrum of a BPLC can be simulated using a modified model originally developed to describe the Bragg reflection of a cholesteric photonic crystal.[2,3] The angle-dependent reflectance for circularly polarized light subject to the circular Bragg effect is given by

$$R = \frac{\kappa^2 (sL)}{s^2 (sL) + \left(\frac{\Delta k}{2}\right)^2 (sL)} \tag{1}$$

where $\kappa = k_0^2 \Delta\varepsilon_{\mathrm{eff}}/(4k)$ is the coupling coefficient proportional to the effective dielectric anisotropy $\Delta\varepsilon_{\mathrm{eff}}$, $s = \sqrt{\kappa^2 - (k-q)^2}$, $k_0 = 2\pi/\lambda$ is the optical wavenumber in vacuum, $k = n_{\mathrm{avg}} k_0$ is the optical wavenumber in the BPLC (proportional to the average refractive index n_{avg}), $q = 2\pi/(\Lambda \cos\varphi)$ is the chirality (inversely proportional to lattice spacing Λ along $\boldsymbol{N}$), and L is the thickness of the BPLC. $\Delta\varepsilon_{\mathrm{eff}}$ is retrieved by fitting the reflection spectrum with Eq. 1. For arbitrary a, b, c, and β,

$$\Lambda = c_0 \times \sqrt{\frac{a^2 + b^2 + c^2}{5c^2/2}} \times \sqrt{\frac{a^2 + (a\tan(\beta) + b\sec(\beta)/2)^2 + (c/2)^2}{a^2 + (b/2)^2 + (c/2)^2}} \tag{2}$$

where c_0 is the c in the BCC symmetry. The second term accounts for the deviation of Λ from c_0 due to lattice distortion. In a BCC lattice, due to its symmetry, $c = b = \sqrt{2}a$, resulting in $a^2 + b^2 + c^2 = 5c^2/2$. Here, $a^2 + b^2 + c^2$ of the distorted lattice is normalized to this reference value $(5c^2/2)$. The last term corrects Λ when $\beta \neq 0$. Also, as φ increases, the reflection band blueshifts. When viewing along $\boldsymbol{N}$, the far-field intensity profile $I(\varphi)$ is calculated by integrating the product of $S(\lambda)$ and $R(\lambda, \varphi)$ over the entire wavelength range: $I(\varphi) = \int S(\lambda) R(\lambda, \varphi) \mathrm{d}\lambda$ [**Fig. S3d**]. The maximum intensity corresponds to the angle at which the Bragg reflection band maximally overlaps with the spectrum of narrowband probe. $I(\varphi)$ thus forms a ring pattern in the Cartesian coordinate system [inset in **Fig. S3d**]. The ring pattern is the same for all four lattice planes, as these planes are equivalent to each other by the symmetry of the lattice.

To generate a Kossel diagram, we project the four intensity profiles I_1–I_4 onto the image plane (aligned perpendicular to the $\boldsymbol{c}$ axis) based on the orientation of the respective lattice planes defined by their normal vectors $\boldsymbol{N}$; we denote the projected intensity profile for lattice plane n as $\widetilde{I_n}$. To determine $\boldsymbol{N}$, we first identify three points (say, Q_1, Q_2, and Q_3) in each lattice plane to form two vectors ($\overrightarrow{Q_1Q_2}$ and $\overrightarrow{Q_1Q_3}$), and the cross product of the two vectors gives the plane normal ($\boldsymbol{N} = \overrightarrow{Q_1Q_2} \times \overrightarrow{Q_1Q_3}$). Following are representative points in crystallographic ($\boldsymbol{abc}$) coordinates for our case [**Fig. S3e**]:
$(a, b/2, 0)$, $(0, b/2, c)$, $(0, 0, c/2)$ in lattice plane 1,
$(a, 0, c/2)$, $(0, b, c/2)$, $(0, b/2, 0)$ in lattice plane 2,
$(a, 0, c/2)$, $(0, b, c/2)$, $(0, b/2, c)$ in lattice plane 3,
$(a, b/2, c)$, $(0, b/2, 0)$, $(0, 0, c/2)$ in lattice plane 4.

Since the $\boldsymbol{a}$ and $\boldsymbol{b}$ axes may not be orthogonal to each other (due to a nonzero skew angle β), these points must be transformed from their crystallographic representation into the laboratory frame (Cartesian coordinates). The transformed points are:
$(a, a\tan(\beta) + b\sec(\beta)/2, 0)$, $(0, b\sec(\beta)/2, c)$, $(0, 0, c/2)$ in lattice plane 1,
$(a, a\tan(\beta), c/2)$, $(0, b\sec(\beta), c/2)$, $(0, b\sec(\beta)/2, 0)$ in lattice plane 2,
$(a, a\tan(\beta), c/2)$, $(0, b\sec(\beta), c/2)$, $(0, b\sec(\beta)/2, c)$ in lattice plane 3,
$(a, a\tan(\beta) + b\sec(\beta)/2, c)$, $(0, b\sec(\beta)/2, 0)$, $(0, 0, c/2)$ in lattice plane 4.
Once the orientation ($\boldsymbol{N}$) of the lattice planes is determined, the simulated Kossel diagram I_{sim} is simply the sum of the intensity profiles projected on the image plane, $I_{\text{sim}} = \sum_n \widetilde{I_n}$ [**Fig. S3f**].

Building upon the numerical simulations described earlier, we now focus on how these simulations are utilized to achieve the best fit with the experimentally measured Kossel diagram. Our primary goal here is to find the optimal values for a, b, and β, which define the simulated diagram. We achieve this by integrating the simulation with an optimization algorithm, such as an interior-point method or genetic algorithm. To ensure proper in-plane alignment between the simulated and measured Kossel diagrams, the simulated diagram is first rotated to maximize the Pearson correlation coefficient with the measured one. The algorithm iteratively refines the simulated Kossel diagram to minimize its total intensity mismatch with the measured diagram. This mismatch is quantified by a cost function, calculated as the sum of absolute intensity differences between corresponding pixels in the two diagrams. As an illustrative example, we explore in **Fig. S4a** the behavior of the cost function with respect to a and b for a tetragonal-crystal case (where $\beta = 0$). Clearly, this optimization problem exhibits convex behavior with a single minimum. The error bar in the fitted lattice parameters is primarily influenced by two factors: the image quality of the measured Kossel diagram and the aberration of the imaging system. The latter can be effectively eliminated through calibration of the imaging system with a well-characterized reflective grating, as described earlier. From the full scan of the parameter space surrounding the optimal lattice constants identified, shown in **Fig. S4a**, the error bar for the lattice constant is estimated to be around ±0.5 nm in our system.

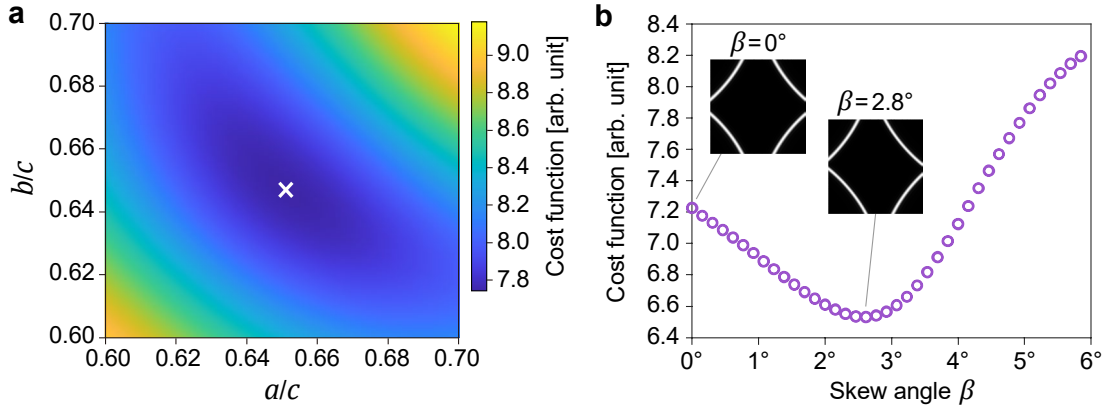

Fig. S4. Kossel-diagram fitting for extracting lattice constants $\boldsymbol{a}$, $\boldsymbol{b}$, and skew angle $\boldsymbol{\beta}$. Cost function is the sum of pixel-wise intensity differences between simulated and measured Kossel diagrams. Prior to fitting, lattice constant c is retrieved from the measured reflection spectrum along the field axis. **a** Cost function values for various combinations of a and b. The experimental Kossel diagram used in the cost function is measured from a tetragonal crystal ($\beta = 0$). White cross marks the optimum solution for a and b (relative to c). **b** Cost function values for different β. A measured Kossel diagram of a monoclinic crystal is used in the cost function. Insets: simulated Kossel diagrams for $\beta = 0°$ and 2.8°. Both **a** and **b** show a convex parameter space with single minimum.

In our code, the optimization begins with $a = c/\sqrt{2}$, $b = c$, and $\beta = 0$ (the cubic-lattice condition), subject to $0 < a \leq b \leq c$ and $-\pi/2 \leq \beta \leq \pi/2$, and typically converges within a few tens of iterations. For monoclinic polycrystals, we first identify one set of four constituent

rings in the measured Kossel diagram and fit it with our numerical model. The skew angle β determines the distortion of the diffraction pattern [right inset in **Fig. S4b**] from its orthorhombic counterpart [left inset in **Fig. S4b**]. **Figure S4b** shows that there exists only one minimum in the parameter space of β while keeping a and b fixed at their optimal values. The other set of Kossel rings exhibits a mirror image. By retrieving β from the other set of Kossel rings, one can find that the two constituent crystals have the same magnitude of β but with opposite signs. Although **Figs. S4a** and **S4b** display only a slice through the parameter space, it is important to note that if the measured Kossel diagram is sufficiently clear, there is only one optimal solution within the parameter space. This unique set of a, b, and β can thus be efficiently determined using conventional optimization algorithms.

Although for the photonic crystals studied here we could safely assume that the $\boldsymbol{c}$ axis is orthogonal to the $\boldsymbol{a}$ and $\boldsymbol{b}$ axes in the fitting process, a more rigorous way of analysis involves treating the angles between any two of the three axes as free parameters. We define the angle between $\boldsymbol{a}$ and $\boldsymbol{b}$ as γ (with $\gamma = 90° - \beta$), the angle between $\boldsymbol{c}$ and $\boldsymbol{a}$ as ζ, and the angle between $\boldsymbol{c}$ and $\boldsymbol{b}$ as α. As previously discussed, simulating a Kossel diagram requires knowing the orientation of the four lattice planes relative to the laboratory frame (Cartesian coordinates), described by their normal vectors $\boldsymbol{N}$. These normal vectors can be determined using three representative points (Q_1, Q_2, and Q_3) on each lattice plane, as shown in **Fig. S3e**. To transform each point $Q = (Q_a, Q_b, Q_c)$ from the crystallographic ($\boldsymbol{abc}$) coordinates to Cartesian coordinates, it is written as a column vector $\boldsymbol{Q} = [Q_a, Q_b, Q_c]^{\mathrm{T}}$ and multiplied by a transformation matrix T:

$$T = \begin{bmatrix} 1 & 0 & 0 \\ \cos\gamma & \sin\gamma & 0 \\ \cos\zeta & \dfrac{\cos\alpha - \cos\zeta\cos\gamma}{\sin\gamma} & \sqrt{1 - \cos^2\zeta - \left(\dfrac{\cos\alpha - \cos\zeta\cos\gamma}{\sin\gamma}\right)^2} \end{bmatrix}. \quad (3)$$

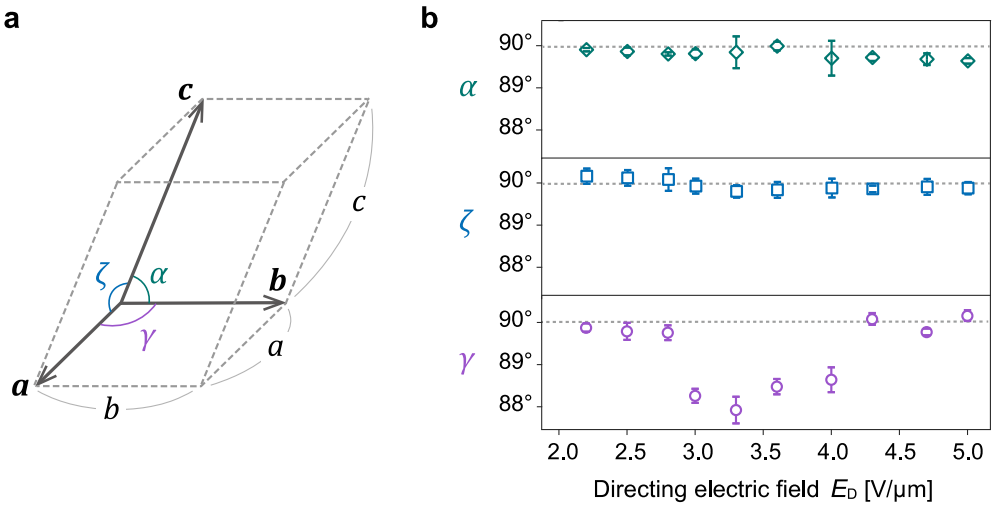

Fig. S5. Complementary analysis to Fig. 5d in main text. a Definition of angles γ ($= 90° - \beta$), ζ, and α. **b** Fitted γ, ζ, and α of monoclinic BPLC as a function of directing-field strength (E_{D}) used in the REDA process. These monoclinic crystals are obtained by directly cooling tetragonal single crystals that are formed by REDA under various E_{D}. Error bars represent the standard deviation.

We incorporate this refined treatment into our code and reanalyze the measured Kossel diagrams of what we previously identified as monoclinic crystals (characterized by $\zeta = \alpha = 90°$ and $\gamma \neq 90°$) [cf. **Fig. 5d**]. These crystals are obtained by two steps: first, REDA of a BPLC under various directing-field strengths (E_{D}) form tetragonal single crystals of different a, b, and c; then, these crystals undergo direct cooling by ~1°C. **Figure S5** shows the fitted

angles γ, ζ, and α as a function of E_{D}, ranging from 2 to 5 V/μm. The fitting process employs a genetic algorithm for optimization, and each data point represents the average of five independent searches. The results show that while ζ and α remain $\sim 90°$ throughout the entire range of analysis, γ varies from $\sim 90°$ (corresponding to $\beta \approx 0°$) to as low as $\sim 88°$ ($\beta \approx 2°$). This confirms our initial characterization of the crystals as monoclinic. Incorporating all six fitting parameters (a, b, c, γ, ζ, α) expands the method's applicability to more intricate systems (e.g., triclinic crystals), but it also increases the computational complexity, time required for fitting, and risk of local optima.

Supplementary References

1. P. Pieranski, E. Dubois-Violette, F. Rothen, and L. Strzelecki. Geometry of Kossel lines in colloidal crystals. *J. Physique* **42**, 53–60 (1981).
2. Hiroyuki Yoshida, Konkanok Anucha, Yasuhiro Ogawa, Yuto Kawata, Masanori Ozaki, Jun-ichi Fukuda, and Hirotsugu Kikuchi. Bragg reflection band width and optical rotatory dispersion of cubic blue-phase liquid crystals. *Phys. Rev. E* **94**, 042703 (2016).
3. Pochi Yeh, and Claire Gu. *Optics of Liquid Crystal Displays*, Chapter 7, Wiley Series in Pure and Applied Optics (2010).